Asian Journal of Chemistry; Vol. 35, No. 8 (2023), 1899-1906

ASIAN JOURNAL OF CHEMISTRY

https://doi.org/10.14233/ajchem.2023.27792

Silver-Alumina Impregnated Maghemite/Magnetite Nanocomposites for Effective Removal of Chromium(VI) from the Tannery Discharge

KISTAN ANDIYAPPAN[1,*] and V. KANCHANA[2]

[1]Department of Chemistry, Panimalar Engineering College, Chennai-600123, India
[2]Department of Chemistry, Sree Sastha Institute of Engineering Technology, Chennai-600123, India

*Corresponding author: E-mail: drakistan14@panimalar.ac.in

Received: 7 April 2023; *Accepted*: 30 June 2023; *Published online*: 31 July 2023; AJC-21323

The chromium(VI) ions present in the tannery waste was efficiently remove by using silver-alumina impregnated maghemite/magnetite nanocomposites as adsorbents. The as-synthesized adsorbents were characterized by XRD, SEM-EDAX, HR-TEM and FT-IR techniques. The adsorption process was found to be pH, time, dosage of adsorbent and temperature dependent. The adsorption data appropriate well with the pseudo-first-order kinetics, pseudo-second-order kinetics Langmuir and Freundlich isotherms. Among the two synthesized nanoabsorbents, the silver-alumina impregnated magnetite (SAMG) nanocomposite was found to be most effective absorbent, and its maximum chromium removal efficiency was achieved to be 98.81% within 2 h at a pH of 3.0 and at dosage of 0.5 g/L.

Keywords: Adsorption, Cr(VI) ion, Tannery effluent, Nanocomposites, Maghemite, Magnetite, Silver alumina magnetite.

INTRODUCTION

Activated sludge technology is widely used in sewage wastewater treatment and increases sludge output, which is difficult to manage economically and environmentally [1-5]. In addition, the conventional treatment techniques have difficulties in terms of process efficiency, time and operating costs. New methods for developing affordable, consumer-friendly, robust, and effective solutions are urgently required due to the global significance of sewage water management and growing demand for water. Based on this assumption, nanotechnology and more specifically magnetic iron oxide nanoparticles (MION), with their large surface-to-volume ratio and magnetic properties, could be one of the best ways to deal with waste [6-10]. Furthermore, it is known that functionalized magnetic nanoparticles exhibit innovative and substantial physico-chemical features, including size, surface charge and particular cooperation with the complex contaminants in wastewater [11-15]. Furthermore, before using nanoparticles on a large scale to treat wastewater or releasing them into the environment, it is critical to assess their toxicity. Although post-treatment solids segregation is the primary drawback of water decontamination using nanoscale materials, the use of magnetically active nanoparticles provides an advantageous and demanding alternative [16-21].

However, tanning production in the Tamilnadu district of Vellore, India contributes to increased water and land chromium pollution. Chromium can exist in both its trivalent and hexavalent forms in water. The second form, however, is especially hazardous since it can cause cancer and genetic issues. People who consume chrome-polluted water are all at risk for gastric abdominal discomfort, epigastric discomfort, biliousness, vomiting, severe diarrhoea, skin degradation, respiratory system problems and lung cancer [22]. In addition to colour, TDS, suspended solids, ammonia, phenols, chlorides and other lourd metals, wastewater produced from these industries also has significantly enhanced concentrations of properties such as colour [23]. Wastewater deposited has usually polluted the surface water and groundwater and increased water overflow is also infected by soil owing to wastewater discharges.

Adsorption is an easy and economy way of removing heavy metals from any aqueous solution. The main benefits of the adsorption method are that single or multiple ions are available in an aqueous solution that is bound to a rigid porous surface and could be projected independently and quantitatviely. Other advantages include low cost, high metal removal efficiency from diluty solutions, minimization of chemical sludge, no additional necessity of nutrients and absorbant redevelopment

and metal retrieval potential [24,25]. Concurrently, suitable magnetic separation topologies are available as a means of enabling and integrating the direct nanoparticle dispersion [26,27]. Compared to traditional column-bed filtration, this method is expected to maximize the surface area of each particle and increase the amount of water that can be taken in by using simple and low-energy equipment.

The development of nanoparticles composed of magnetized phases, whether it is for direct usage as actvie phases or indirect use as a support in the removal of pollutants is of great interest. This investigation focuses on the rapid treatment of tannery wastewaters with the aim of maximum removal of Cr(VI) and other contaminants present in tannery effluent using two different magnetized phases nanocomposites *viz.* maghemite (BMH), magnetite (BMG), silver alumina magnetite (SAMG) and silver alumina maghemite nanocomposite (SAMH) that have been synthesized. Adsorption studies using different nanocomposites as effective adsorbents were determined in order to determine the impact of various experimental parameters.

EXPERIMENTAL

In order to synthesize nanoparticles, the chemical reagents and chemicals were purchased from Sigma-Aldrich, India and used as received. For absorbance measurements, Shimadzu (DTG 60 H) (UV-Vis) spectrophotometer with a 1 cm quartz cell was used. A pH metre from EuTech was used to determine the pH of the solution.

Synthesis of silver alumina nanoparticles: Silver-alumina nanoparticles were prepared through chemical reduction. In most experiments, 500 mL of 1×10^{-3} M $AgNO_3$ was allowed to boil followed by the addition of 5 mL of trisodium citrate gradually. The colour of the solution did not alter until after it had been heated for 2 h to a pale yellow and then cool to room temperature. In order to facilitate the saturated adsorption of nanoparticles to a dry-cleaned and dried surface, 5 g of alumina were soaked, agitated and stored for 6 h.

Synthesis of maghemite nanoparticles (BMH): The mixed maghemite was synthesized using the conventional chemical co-precipitation method. The solution was bubbled for 20 min with N_2 gas followed by the addition of 0.4 mol of $FeCl_3 \cdot 6H_2O$ and 0.2 mol of $FeCl_2 \cdot 4H_2O$. The pH was then adjusted to 10 by adding 50 mL of 4 mol L^{-1} NH_3 solution. The solution was heated at 85 ºC for 40 min. The formed black nanoparticles were eliminated by an external magnetic field and neutralized by ultrapure water. The obtained nanoparticles were baked for 1 h at 300 ºC to generate the magnet iron oxide nanoparticles with a reddish-brown colour.

Synthesis of silver alumina maghemite nanocomposite (SAMH): Maghemite nanoparticles (BMH, 5 g) was mixed with 5 g of silver alumina nanoparticles to obtain a finely grain silver alumina maghemite nanocomposite material.

Synthesis of magnetite nanocomposite (BMG): Magnetite nanocomposite was prepared by a sol-gel technique. A brown gel was obtained by dissolving 0.04 mol ferric nitrate in 25 mL of ethylene glycol using a magnetic stirrer for 2.25 h at 60 ºC and then dried at 250 ºC in an oven for 2 h. After drying, the xerogel was heated at temperatures between 300 and 350 ºC.

Synthesis of silver alumina magnetite nanocomposite (SAMG): Magnetite nanocomposite (BMG, 5 g) was prepared mixed thoroughly with 5 g of silver alumina nanoparticles to obtain a finely grain silver alumina magnetite nanocomposite material.

Preparation of tannery effluent by digestion: In a beaker, 50 mL of effluent and 15 mL of conc. HNO_3 were mixed thoroughly and then concentrate the solution at 60-75 ºC to reduce its contents to half its volume followed by the addition of 7.5 mL of $HClO_4$ dropwise with constant stirring and heated again for 2 h at the same temperature. The sample was then diluted with the same quantity of solution with distilled water. The digested sample concentration was then measured by AAS.

RESULTS AND DISCUSSION

FT-IR studies

In maghemite nanoparticles, the band at 3500-3000 cm^{-1} which is the attributed due to the hydroxyl groups (OH *str.*), whereas the peaks at 1764 and 1633 cm^{-1}, which are due to the fundamental and overtone O-H stretching vibrations of hydroxyl groups of BMH and SAMH nanocomposites, respectively. Additionally, the band at 603-430 cm^{-1} appears due to the metal-oxide (Fe-O) stretching bands (Fig. 1a-b).

The characteristic bands at 3425 and 3417 cm^{-1} correspond to the hydroxyl groups (OH *str.*) of BMG and SAMG, respectively (Fig. 1c-d). In the region at 1680-1625 cm^{-1} (in BMG) and 1638-1618 cm^{-1} (in SAMG) were due to the fundamental and overtone O-H stretching vibrations. Another peak appears at 551-460 cm^{-1} region correspond to the Fe-O bond, while in case of silver alumina magnetite nanocomposite, this peak appeared at 538-463 cm^{-1}.

XRD studies

A X-ray diffraction was used to analyze the crystal structure of synthesized maghemite nanoparticles (BHM) and its silver alumina nanocomposite (SAMH). In the X-ray diffraction pattern of maghemite nanoparticles and silver alumina maghemite nanocomposite, the sharp peaks and broad diffraction points were observed as 2θ 31.83º and 31.75º, respectively (Fig. 2a-b). The typical grain size of maghemite nanoparticles and silver alumina maghemite (SAMH) nanocomposite was found to be 15 nm and 10 nm, respectively.

In case of BMG and SAMG adsorbents, the magnetite nanoparticles and silver alumina magnetite nanocomposite, the sharp peaks and broad diffraction points were observed as 2θ 35.66º and 35.68º, respectively (Fig. 2c-d). In a similar manner, it was found that the usual grain size of magnetite nanoparticles (BMG) and silver alumina magnetite (SAMG) nanocomposite had been 12 nm and 7 nm, respectively.

SEM studies

From the SEM images (Fig. 3a-b), it was observed that the synthesized magnetite nanoparticles were of non-uniform size and shape, while the SEM image of silver alumina magnetite (SAMH) nanocomposite indicated that the material is agglomerated. The EDAX analysis showed that the synthesized nano-

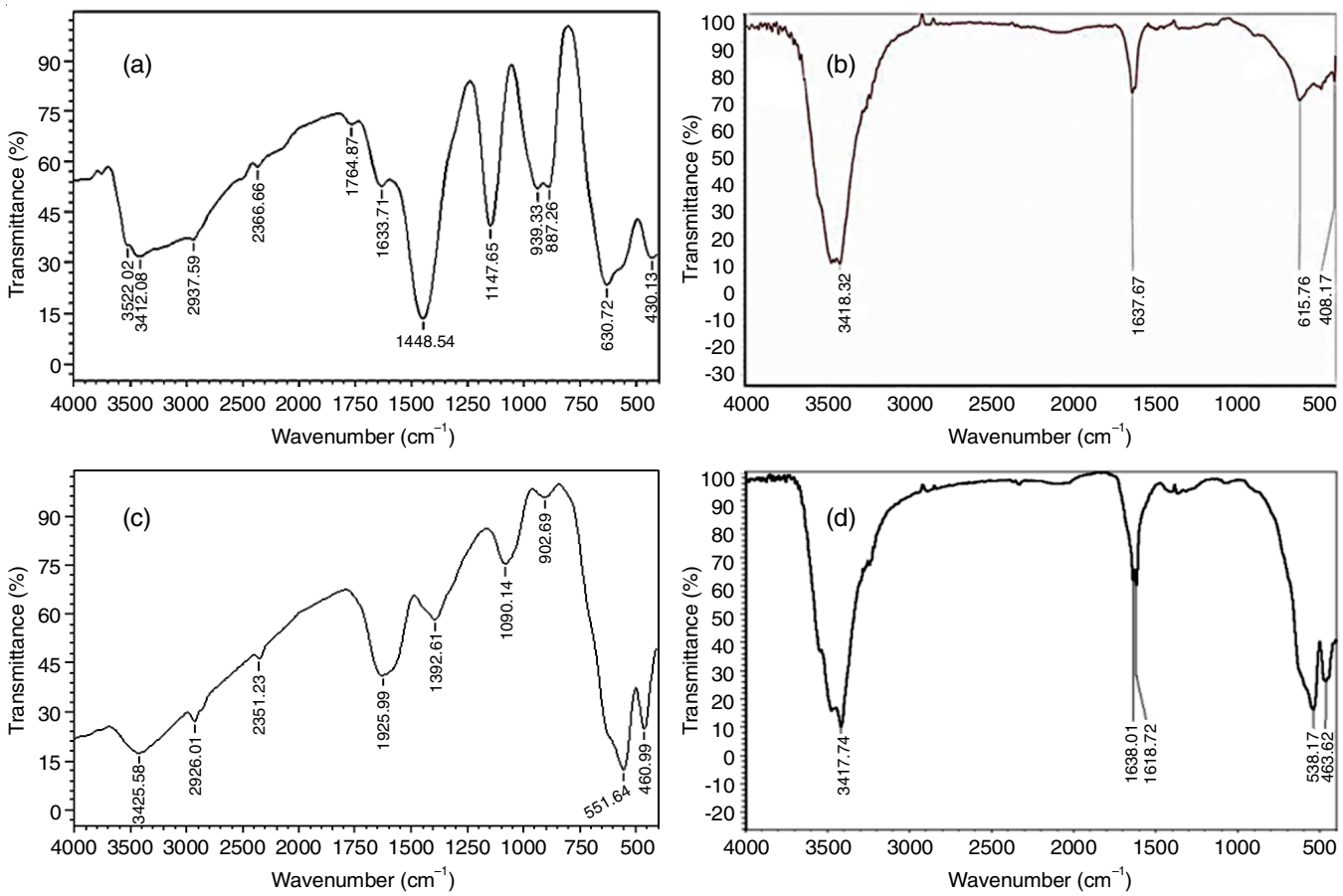

Fig. 1. FT-IR spectra of (a) maghemite nanoparticles (BMH); (b) silver alumina impregnated maghemite nanocomposite (SAMH); (c) magnetite nanoparticles (BMG) and (d) silver-alumina impregnated magnetite nanocomposite (SAMG)

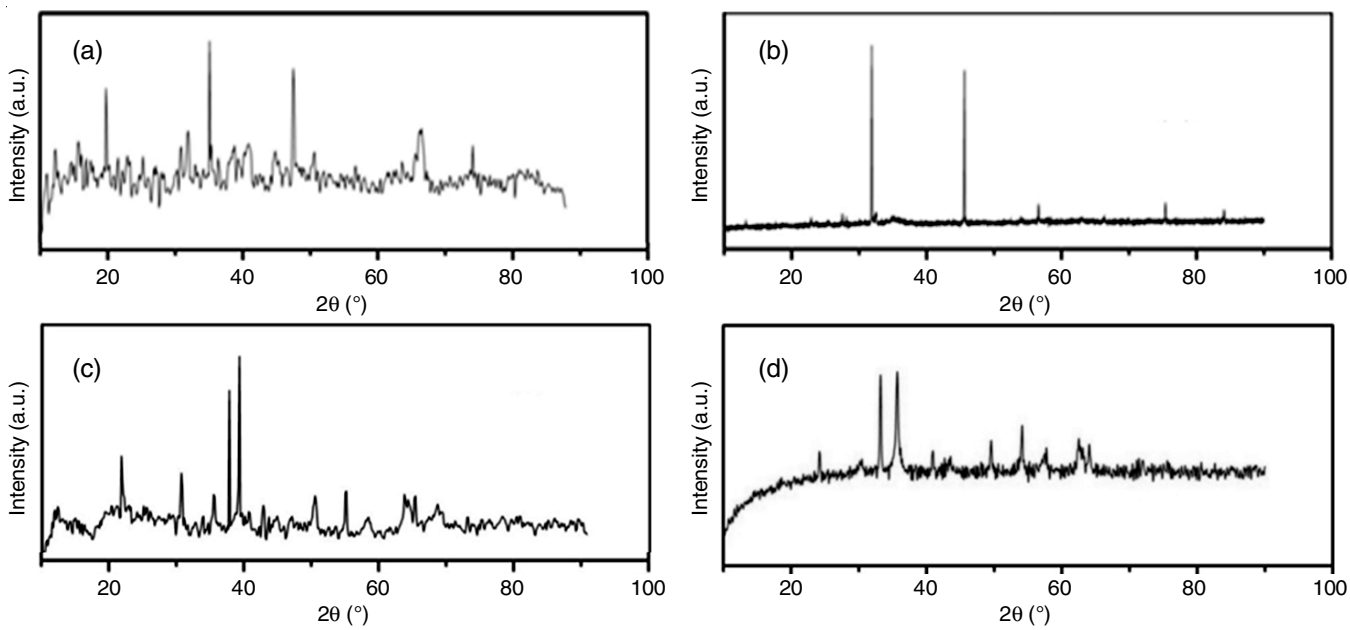

Fig. 2. XRD spectra of (a) maghemite nanoparticles (BMH); (b) silver alumina impregnated maghemite nanocomposite (SAMH); (c) magnetite nanoparticles (BMG) and (d) silver-alumina impregnated magnetite nanocomposite (SAMG)

composite consists of only iron and oxygen. The nanocomposite (BMH) had 45.60% iron and 31.11% oxygen by mass. Other impurities such as sodium and chloride were also identified (Fig. 3c), which might be due to the insufficient washing during the synthesis. The EDAX displays the spectrum of silver alumina magnetite (SAMG), which comprises silver, iron, aluminium and oxygen having the weight proportion of 2.04, 3.04, 46.85 and 47.98% (Table-1).

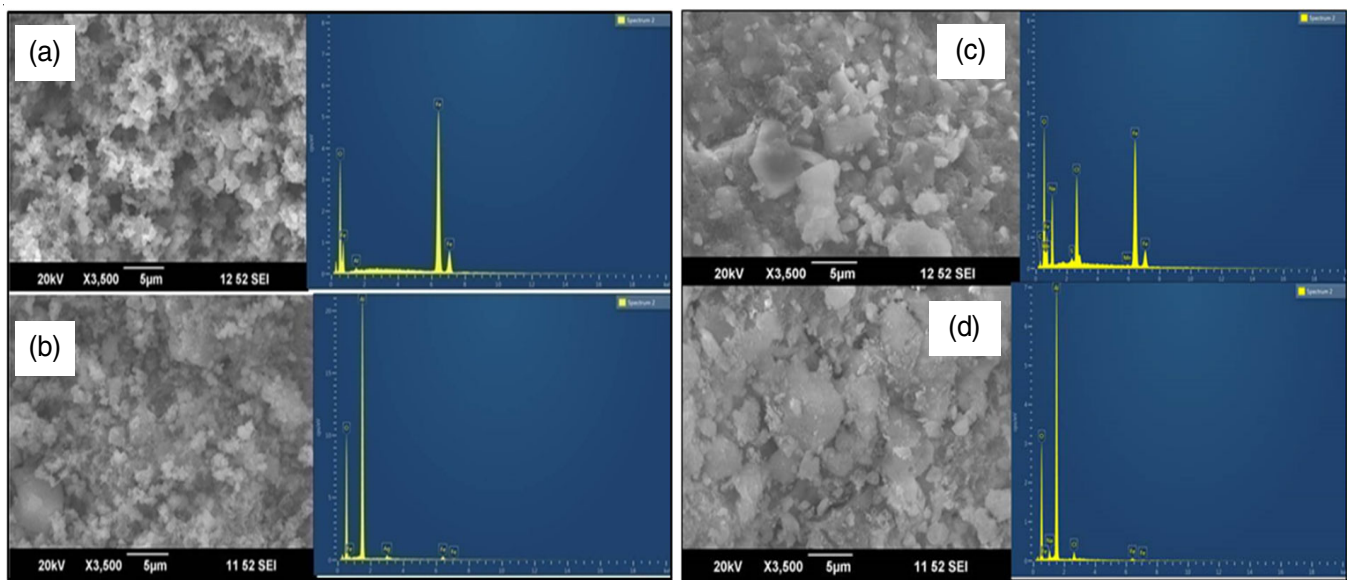

Fig. 3. SEM-EDAX images of (a) maghemite nanoparticles (BMH); (b) silver alumina impregnated maghemite nanocomposite (SAMH); (c) magnetite nanoparticles (BMG) and (d) silver-alumina impregnated magnetite nanocomposite (SAMG)

TABLE-1
ELEMENTAL COMPOSITION DATA OF MAGNETITE NANOPARTICLES AND SILVER ALUMINA MAGNETITE (SAMG) NANOCOMPOSITE

BMG			SAMG		
Element	Mass (%)	Atom (%)	Element	Mass (%)	Atom (%)
O	20.23	46.76	O	50.34	64.54
Fe	79.77	53.24	Ag	2.32	0.44
			Al	44.88	34.12
			Fe	2.47	0.91
Total	100	100	Total	100	100

In case of BMG nanocomposite, the magnetite nanoparticles were of non-uniform size and shape (Fig. 3c). The SEM image of synthesized magnetite nanoparticles matched well to those reported in the previous literature [28]. However, silver alumina magnetite (SAMG) nanocomposites were agglomerated in nature (Fig. 3d). The EDX results revealed that only iron and oxygen are present in the synthesized magnetite nanoparticles and the concentration of iron was 79.77%while that of oxygen was 20.23%. In case of SAMG nanocomposite, the EDX results revealed the presence of silver, iron, aluminum and oxygen having the mass percentage of 2.32%, 2.47%, 44.8% and 50.34%, repectively.

TEM studies

The synthesized BMH nanoparticles displayed a spherical and hexagonal shapes. The BMH nanocomposite particles have been finely separated and thoroughly distributed as observed in Fig. 4a. In case of SAMH, a nanocomposite reveals the formation of nanorods (Fig. 4b). The maghemite and silver alumina maghemite nanocomposites have particle sizes of around 29 nm and 18 nm, respectively.

The synthesized maghemite nanoparticles (BMH) displays the spherical shape and the matrix was also uniformly shaped oval (Fig. 4c). Moreover, BMH nanoparticles in silver alumina are finely dispersed as revealed in Fig. 4d. The particle size of

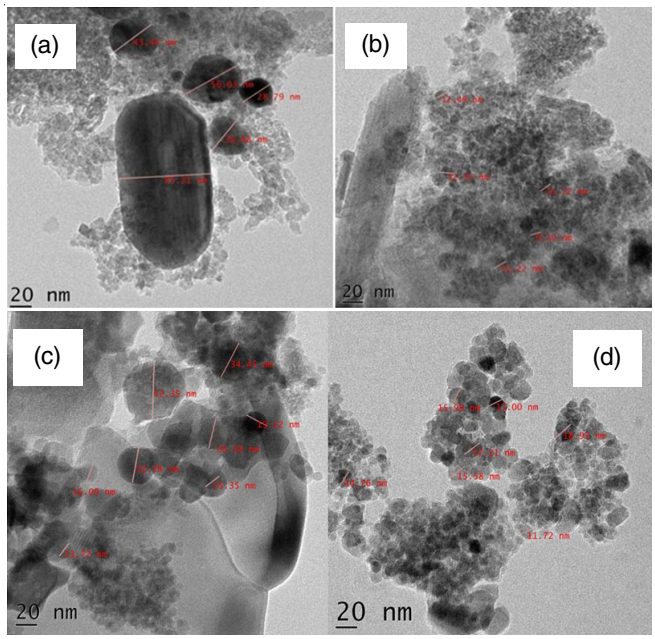

Fig. 4. HRTEM images of (a) maghemite nanoparticles (BMH); (b) silver alumina impregnated maghemite nanocomposite (SAMH); (c) magnetite nanoparticles (BMG) and (d) silver-alumina impregnated magnetite nanocomposite (SAMG)

the magnetite nanocomposite and BMH incorporated silver alumina nanocomposite were of 26 and 15 nm, respectively.

Optimization of the adsorption parameters

Effect of pH: For chromium(VI) adsorption from the tannery effluent, pH is one of the most important parameters because it controls the surface load, the amount of adsorption and the type of adsorbent. In order to assess the effect of pH on chromium(VI) sorption, batch experiments were conducted at a range of pH values from 2 to 9. The maximal intake of Cr(VI) was reached at maximum pH 2-3 and a higher pH, and the rate of Cr(VI) removal was determined for SAMH and SAMG nano-

composites at 90% and 92%, respectively. Fig. 5 shows the results of the adsorption rate and Cr(VI) elimination at initial concentration of (mg/L) at different pHs.

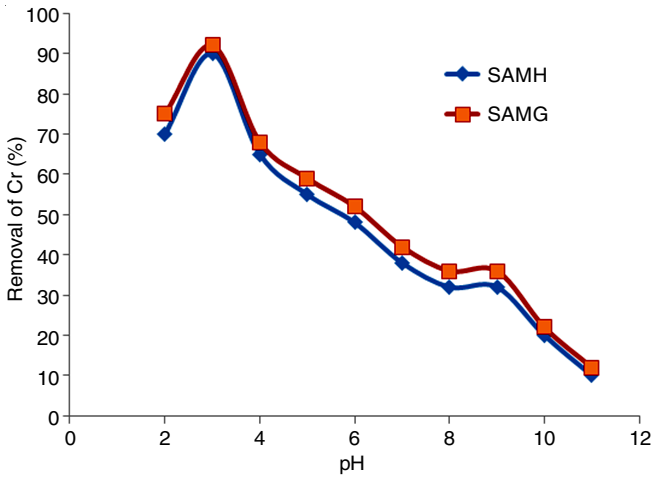

Fig. 5. Influence of pH on chromium(VI) adsorption

Effect of adsorbent dose: The adsorption of Cr(VI) onto an adsorbent was studied by changing the amount of adsorbent from 0.1 to 0.5 g while keeping the initial pH (50 ppm/L) and contact time constant (Fig. 6). The optimal removal of Cr(VI) with 0.5 g of adsorbent was identified, which is attributed due to the high availability of adsorption sites resulting from the increase in effective surface area caused by the increasing dose of adsorbents or the adsorbent aggregation. The number of accessible adsorption sites reduces as sorbent concentration increases, yet removal efficiency increases. It is reasonable to expect that as the amount of adsorbent used increases, the removal processes will become more effective.

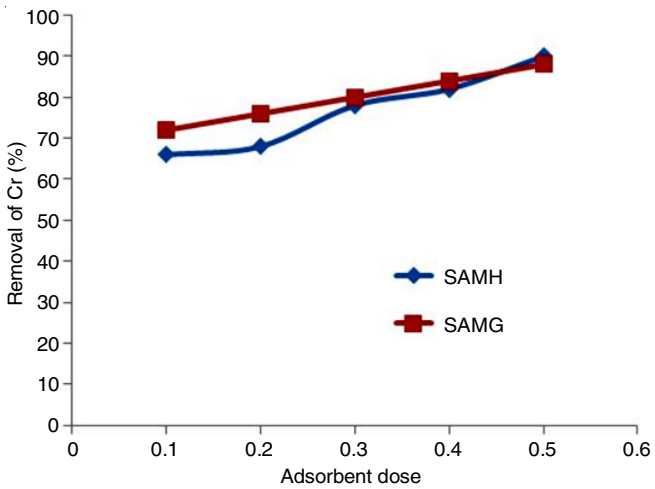

Fig. 6. Adsorption of chromium(VI): SAMH *vs.* SAMG

Effect of time: For increasing the contact time, an adsorption of Cr(VI) was developed and achieves an equilibrium after 100 min. Even though a greater volume for Cr(VI) could be obtained, Fig. 7 demonstrates an increase in productivity as contact time reduces, resulting in a more desirable complex composite. An optimal period for full processing was 100 min,

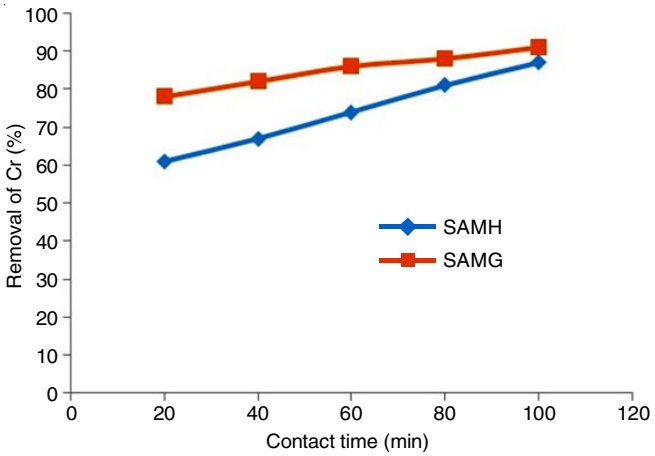

Fig. 7. Contact time on the adsorption of chromium(VI): SAMH *vs.* SAMG

91% (SAMH) and 91% (SAMG). To order to additional refine certain factors, the touch period was found to correlate to the adsorbent and adsorbent as the balancing time.

Effect of initial concentration: An adsorption studies with specific chromium ion concentrations within the limit of 500, 250, 200, 100 and 50 ppm found that the percentage of the elimination of Cr(VI) decreased, with the chromium ion concentration increasing. The peak Cr(VI) ingestion in nanocomposite was obtained at the initial ion concentration of 0.5 mg/L, but decrease in the higher concentrations, leading to enhancing binding site saturation. It is easy to observe a shift when the solution concentration increases and more Cr(VI) is delivered to the contact and adsorbed (Fig. 8).

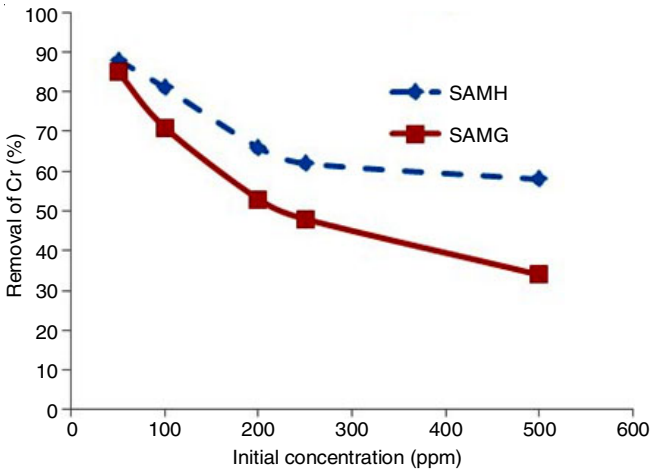

Fig. 8. Initial concentration effect on the adsorption of chromium(VI): SAMH *vs.* SAMG

Kinetics studies: Using pseudo-first-order and pseudo-second-order kinetics, the adsorption kinetics of chromium(VI) on synthesized nanocomposites were examined [29,30].

Pseudo-first-order: The equation represents the linearized form of the pseudo-first-order Lagergren equation:

$$\log(q_e - q_t) = \log q_e - \left(\frac{k_1}{2.303}\right)t \quad (1)$$

where q_e and q_t are the quantity of Cr(VI) adsorption (mg/g) at equilibrium and at time 't' (min), and k_1 (min^{-1}) is the

adsorption rate constant of the pseudo first-order. The linear plots of log ($q_e - q_t$) *versus* t are shown in Fig. 9.

Pseudo-second-order: The linearized equation of the pseudo-second-order rate can be represented as:

$$\frac{t}{q_t} = \frac{1}{K_2 q_e^2} + \frac{t}{q_e} \quad (2)$$

where the concentrations of q_e and q_t are dye adsorbed (mg/g) at the equilibrium and 't' (min), respectively and k_2 (g mg^{-1}, min^{-1}), there is no difficulty in assigning efficient q_e since q_e and k_2 can be determined [30-32] from the slope and intercept.

The values of K_1 may be computed from the linear slope log plot (q_e–q_t) *vs.* t and K_2 can be obtained from the linear slope plot t/q_t *versus* t. The correlation coefficient (R^2) and values of k_1, k_2, q_e, are presented in Table-2. Pseudo-second order linear plots produced greater R^2 values as compared to pseudo-first order linear plots (Fig. 10). The pseudo-second order values of q_e (cal) were closer to q_e (exp) than the pseudo-first order values, which suggest that the pseudo-second-order model is more effective [32-34].

Adsorption studies: Adsorption methods for removing the heavy metal ions from aqueous solutions depend extensively on the equilibrium isotherm throughout the design and

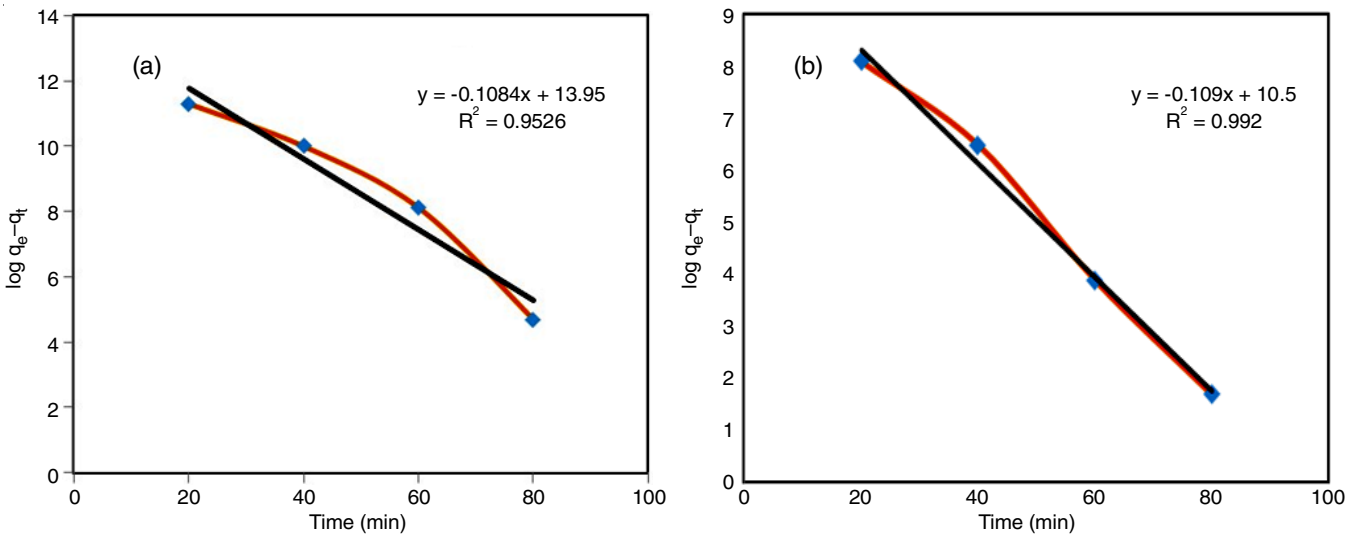

Fig. 9. Pseudo-first-order adsorption curve of chromium(VI) using SAMH (a) and SAMG (b) nanocomposites

TABLE-2
LAGERGREN'S PSEUDO-FIRST-ORDER AND PSEUDO-SECOND-ORDER KINETIC MODELS FOR THE ADSORPTION OF CHROMIUM(VI) ON SAMH AND SAMG NANOCOMPOSITES WERE COMPARED

Adsorbent	Pseudo first order kinetic model			Experimental value	Pseudo-second order kinetic model		
	q_e (mg/g)	K_1 (min^{-1})	R^2	q_e (mg/g)	q_e (mg/g)	K_2 (min^{-1})	R^2
SAMH	1.548	0.2487	0.952	46.0	2.128	0.6734	0.988
SAMG	3.162	0.2510	0.992	44.5	1.303	5.122	0.998

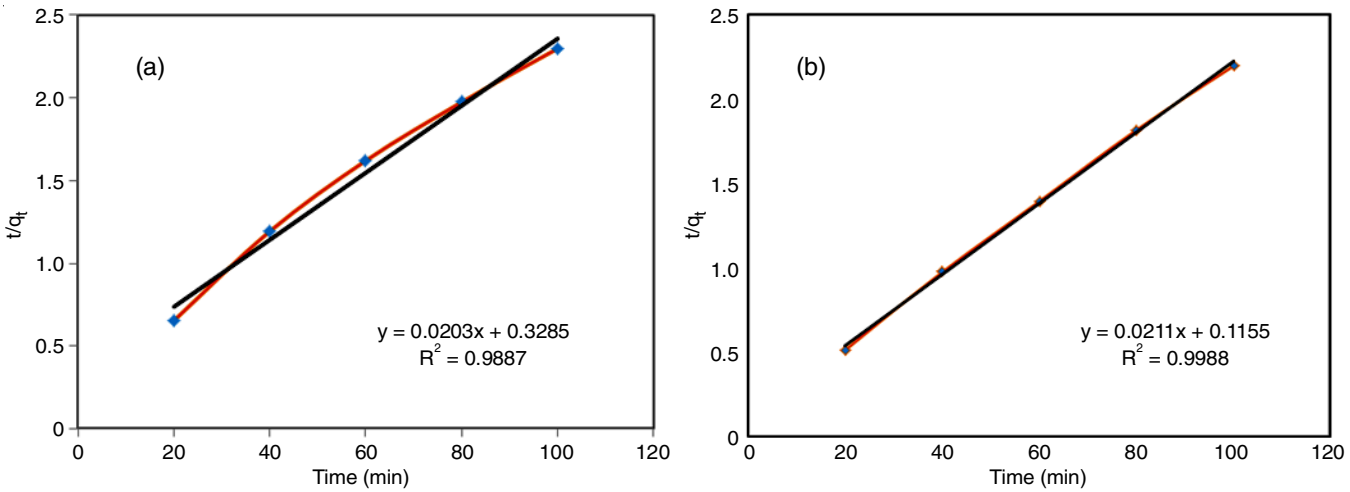

Fig. 10. Pseudo-second-order adsorption curve of chromium(VI) using SAMH (a) and SAMG (b) nanocomposites

TABLE-3
DISTRIBUTION DATA FOR THE ADSORBENT AND THE ADSORBATE OF SAMH AND SAMG NANOCOMPOSITES

	SAMH					SAMG			
Initial concentration of Cr(VI) in 50 ppm	50	100	200	250	500	–	–	–	–
Equalent adsorption in 0.5 g of sorbent (q_e)	46	84	142	166	312	44.5	73	110	126
Amount of Cr(VI) left in solution (c_e)	4	16	58	84	188	5.5	27	90	124
C_e/q_e	0.086	0.190	0.408	0.506	0.602	0.1235	0.369	0.8181	0.984

adsorption processes. In this current work, two well-adsorption process defined by Langmuir and Freundlich isotherms are considered. The conditions for the adsorption studies of Cr(VI) using silver-alumina impregnated maghemite/magnetite nanocomposites are given in Table-3.

Langmuir isotherm: Langmuir's equation defines the monolayer adsorption. This model is based on the idea that there is only one layer of solute adsorption at a constant temperature and a uniform adsorption energy. The linear form of Langmuir isotherm may be represented as:

$$\frac{C_{eq}}{C_{ads}} = \frac{bC_{eq}}{K_L} + \frac{1}{K_L} \quad (3)$$

$$C_{max} = \frac{K_L}{b} \quad (4)$$

where C_{ads} = The quantity of solute absorbed per unit of adsorbent mass (mg/g); C_{eq} = the equilibrium solute concentration in the bulk solution (mg/m^3); C_{max} = The monolayer adsorption capacity (mg/g) and K_L = the sorption equilibrium constant, are proportional to the adsorption free energy.

To analyze the applicability of Langmuir isotherm for adsorption of SAMH nanocomposite, the significance of $K_L$and C_{max} is illustrated with a linear plot of C_e/q_e against C_e. Table-4 displays the values of C_{max}, K_L and R^2. The separation factor ($R_L < 1$) value for Cr(VI) on to SAMH and designates that adsorption in this study was satisfactory (Table-5).

TABLE-4
ADSORPTION ISOTHERM CONSTANTS CONSTANT, C_{max} AND CORRELATION COEFFICIENTS SAMH AND SAMG

Adsorbent	K_L (dm^3/g)	b (dm^3/g)	C_{max} (mg/g)	R^2
SAMH	5.813	0.0116	500.11	0.818
SAMG	3.952	0.0158	250.12	0.957

Freundlich isotherm: According to the Freundlich model, adsorption at the surface is not the rate-limiting phase because the energies of adsorbent sites vary exponentially. The Freundlich isotherm is based on the fact that heat doesn't spread out in the same way when it moves from the atmosphere to a surface made of different materials. The Freundlich isotherm can be represented as:

$$q_e = K_f C_e^{1/n} \quad (5)$$

TABLE-5
BASED ON LANGMUIR ADSORPTION, R_L VALUES (SAMH AND SAMG)

Adsorbent	Concentration of Cr(VI) (mg/L)		R_L value
	Initial	Final	
SAMH	50	4	0.957
	100	16	0.850
	200	58	0.610
	250	84	0.519
	500	188	0.483
SAMG	50	5.5	0.924
	100	27	0.711
	200	90	0.425
	250	124	0.349
	500	315	0.174

where K_f is the adsorption capacity per unit concentration (L/g) and 1/n is the adsorption intensity. The 1/n values show whether an isotherm is irreversible (1/n = 0), favourable (0 < 1/n < 1)), or unfavourable (1/n > 1) based on its reversibility. An equation can be rearranged into a linear form, which can be represented as follows:

$$\log q_e = \log K_f + \frac{1}{n}\log C_e \quad (6)$$

where C_e is the equilibrium concentration (mg/m^3) and q_e is the amount adsorbed per unit mass of adsorbent (mg/g). When ln q_e was plotted against ln C_e, a straight line was obtained, which shows that Cr(VI) binds well according to the Freundlich isotherm. The applicability of the Freundlich model for adsorption on SAMH and SAMG nanocomposite adsorbents, a linear plot of log q_e *vs.* log C_e was constructed and Table-6 displays the values for K_f, n and R_2.

The value of n, ranging between 1-10, suggests that the adsorption is beneficial. The numerical value of 1/n < 1 implies the adsorption efficiency at lower equilibrium rates is only reduced slightly. This isotherm does not estimate the adsorbent's saturation. Therefore, the statistical projections of infinite surface penetration suggest the multilayer surface adsorption. The findings of the present study reveal that the Freundlich model has more R^2 than the Langmuir model, thus in present case, the adsorption results suit the Freundlich isotherm very well. As shown by the R_L value, The Cr(VI) adsorption was effective in this study.

TABLE-6
COMPARISON BETWEEN LANGMUIR ISOTHERM AND FREUNDLICH ISOTHERM FOR Cr(VI) ADSORPTION ON SAMH AND SAMG

Adsorbent	Langmuir constants				Freundlich constants		
	K_L (dm^3/g)	B (dm^3/g)	C_{max} (mg/g)	R^2	K_f (dm^3/g)	n (dm^3/g)	R^2
SAMH	5.813	0.0116	500.11	0.818	4.025	2.114	0.980
SAMG	3.952	0.0158	250.12	0.957	3.018	2.873	0.995

Conclusion

Two newly synthesized nanocomposite adsorbents silver alumina maghemite (SAMH) and silver alumina magnetite (SAMG) were found to be effective for the removal of Cr(VI) from tannery effluent which is attributed due to their high adsorption efficiency, large surface area and microporous structure. The results showed that at the optimum conditions of adsorbent dose of 0.5 g/L, contact period of 120 min, and pH = 3, the maximum 98.81% removal efficiency of Cr(VI) was achieved from the tannery effluent. The adsorption data suitable with the pseudo-first-order kinetics, pseudo-second-order kinetics Langmuir and Freundlich isotherm equation. The adsorption ability increased with the increasing contact time, amount of adsorbent and low pH.

CONFLICT OF INTEREST

The authors declare that there is no conflict of interests regarding the publication of this article.

REFERENCES

1. U.O. Aigbe and O.A. Osibote, *J. Environ. Chem. Eng.*, **8**, 104503 (2020); https://doi.org/10.1016/j.jece.2020.104503
2. O. Agboola, O.S.I. Fayomi, A. Ayodeji, A.O. Ayeni, E.E. Alagbe, S.E. Sanni, E.E. Okoro, L. Moropeng, R. Sadiku, K.W. Kupolati and B.A. Oni, *Membranes*, **11**, 139 (2021); https://doi.org/10.3390/membranes11020139
3. P. Sharma, D. Dutta, A. Udayan and S. Kumar, *J. Environ. Chem. Eng.*, **9**, 106673 (2021); https://doi.org/10.1016/j.jece.2021.106673
4. M.K. Bharti, S. Gupta, S. Chalia, I. Garg, P. Thakur and A. Thakur, *J. Supercond. Nov. Magn.*, **33**, 3651 (2020); https://doi.org/10.1007/s10948-020-05657-1
5. K.Z. Elwakeel, A.M. Elgarahy, Z.A. Khan, M.S. Almughamisi and A.S. Al-Bogami, *Mater. Adv.*, **1**, 1546 (2020); https://doi.org/10.1039/D0MA00153H
6. M.J. Hato, T.C. Maponya, K.E. Ramohlola, K.D. Modibane, A. Maity, G.R. Monama, K. Makgopa and A. Bello, Polymer-Based Magnetic Nanocomposites for the Removal of Highly Toxic Hexavalent Chromium from Aqueous Solutions, In: Advanced Nanostructured Materials for Environmental Remediation, Springer International Publishing, Chap. 8, pp. 189-227 (2019).
7. N.R. Mizyed, *Environ. Sci. Policy*, **25**, 186 (2013); https://doi.org/10.1016/j.envsci.2012.10.016
8. B. Tansel, *Recent Pat. Chem. Eng.*, **1**, 17 (2008); https://doi.org/10.2174/2211334710801010017
9. S. Liu, Y. Gu, S. Wang, Y. Zhang, Y. Fang, D.M. Johnson and Y. Huang, *Chin. Sci. Bull.*, **58**, 2340 (2013); https://doi.org/10.1007/s11434-013-5784-4
10. M.M. Kabir, N. Nahar, M.M. Akter, F. Alam, B.H. Gilroyed, M.M. Misu, M. Didar-ul-Alam, M. Hakim, L. Tijing and H.K. Shon, *J. Water Process Eng.*, **52**, 103578 (2023); https://doi.org/10.1016/j.jwpe.2023.103578
11. M.M. da Silva, J.M.W. Duarte Neto, B.V. Barros Regueira, M.T.T. do Couto, R.V. da Silva Sobral, A.E. Sales Conniff, R.M.P. Brandão Costa, M.C. de B. Lira Nogueira, N.P. da Silva Santos, L. Pastrana, A.C. Lima Leite, A. Converti, T.P. Nascimento and A.L. Figueiredo Porto, *Protein Expr. Purif.*, **192**, 106044 (2022); https://doi.org/10.1016/j.pep.2022.106044
12. J. Fito, M. Abewaa and T. Nkambule, *Appl. Water Sci.*, **13**, 78 (2023); https://doi.org/10.1007/s13201-023-01880-y
13. S.C.N. Tang and I.M.C. Lo, *Water Res.*, **47**, 2613 (2013); https://doi.org/10.1016/j.watres.2013.02.039
14. A.T. Abeto, B.S. Mustafa, B.A. Bekele and K.W. Firomsa, *J. Environ. Public Health*, **2023**, 5663261 (2023); https://doi.org/10.1155/2023/5663261
15. C. Baresel, V. Schaller, C. Jonasson, C. Johansson, R. Bordes, V. Chauhan, A. Sugunan, J. Sommertune and S. Welling, *Heliyon*, **5**, e02325 (2019); https://doi.org/10.1016/j.heliyon.2019.e02325
16. J. Fito, S. Tibebu and T.T. Nkambule, *BMC Chem.*, **17**, 4 (2023); https://doi.org/10.1186/s13065-023-00913-6
17. A. Kalsoom, N. Jamil, S.M.U. Hassan, J.A. Khan and R. Batool, *Curr. Microbiol.*, **80**, 99 (2023); https://doi.org/10.1007/s00284-023-03194-3
18. X. Qu, P.J.J. Alvarez and Q. Li, *Water Res.*, **47**, 3931 (2013); https://doi.org/10.1016/j.watres.2012.09.058
19. M.D. Yahya, K.S. Obayomi, M.B. Abdulkadir, Y.A. Iyaka and A.G. Olugbenga, *Water Sci. Eng.*, **13**, 202 (2020); https://doi.org/10.1016/j.wse.2020.09.007
20. Ö. Madenli, C. Akarsu and E.Ü. Deveci, *Ceram. Int.*, **49**, 16440 (2023); https://doi.org/10.1016/j.ceramint.2023.02.005
21. T. Rasheed, *J. Clean. Prod.*, **362**, 132338 (2022); https://doi.org/10.1016/j.jclepro.2022.132338
22. M. Tumolo, V. Ancona, D.D. Paola, D. Losacco, C. Campanale, C. Massarelli and V.F. Uricchio, *Int. J. Environ. Res. Public Health*, **17**, 5438 (2020); https://doi.org/10.3390/ijerph17155438
23. K. Sathya, K. Nagarajan, G.C. Geor Malar, S. Rajalakshmi and P. Raja Lakshmi, *Appl. Water Sci.*, **12**, 70 (2022); https://doi.org/10.1007/s13201-022-01594-7
24. S. Rajendran, A.K. Priya, P. Senthil Kumar, T.K.A. Hoang, K. Sekar, K.Y. Chong, K.S. Khoo, H.S. Ng and P.L. Show, *Chemosphere*, **303**, 135146 (2022); https://doi.org/10.1016/j.chemosphere.2022.135146
25. R. Yousef, H. Qiblawey and M.H. El-Naas, *Processes*, **8**, 1657 (2020); https://doi.org/10.3390/pr8121657
26. T.A. Aragaw, F.M. Bogale and B.A. Aragaw, *J. Saudi Chem. Soc.*, **25**, 101280 (2021); https://doi.org/10.1016/j.jscs.2021.101280
27. F.F. Lo, K.-W. Kow, F. Kung, F. Ahamed, P.-L. Kiew, S.-P. Yeap, H.-S. Chua, C.-H. Chan, R. Yusoff and Y.K. Ho, *Sci. Total Environ.*, **780**, 146337 (2021); https://doi.org/10.1016/j.scitotenv.2021.146337
28. E.A. Setiadi, Rahmat, S. Simbolon, M. Yunus, C. Kurniawan, A.P. Tetuko1, S. Zelviani, Rahmaniah and P. Sebayang, *J. Phys.: Conf. Ser.*, **979**, 012064 (2018); https://doi.org/10.1088/1742-6596/979/1/012064
29. F. Moradnia, S.T. Fardood, A. Ramazani, B. Min, S.W. Joo and R.S. Varma, *J. Clean. Prod.*, **288**, 125632 (2021); https://doi.org/10.1016/j.jclepro.2020.125632
30. Z. Akchiche, A.B. Abba and S. Saggai, *Algerian J. Chem. Eng.*, **1**, 8 (2021); https://doi.org/10.5281/zenodo.4458444
31. T. Castelo-Grande, P.A. Augusto, J. Rico, J. Marcos, R. Iglesias, L. Hernández and D. Barbosa, *J. Environ. Manage.*, **281**, 111872 (2021); https://doi.org/10.1016/j.jenvman.2020.111872
32. T. Castelo-Grande, P.A. Augusto, J. Rico, J. Marcos, R. Iglesias, L. Hernández and D. Barbosa, *J. Environ. Manage.*, **285**, 112177 (2021); https://doi.org/10.1016/j.jenvman.2021.112177
33. M.A. Kiser, P. Westerhoff, T. Benn, Y. Wang, J. Pérez-Rivera and K. Hristovski, *Environ. Sci. Technol.*, **43**, 6757 (2009); https://doi.org/10.1021/es901102n
34. Y.K. Gun'ko and D.F. Brougham, in Eds.: S.R. Kumar, Magnetic Nanomaterials as MRI Contrast Agents, In: Magnetic Nanomaterials, John Wiley & Sons, Inc. (2009).